Performance of the MICE diagnostic system

The MICE Collaboration

Abstract

Muon beams of low emittance provide the basis for the intense, well-characterised neutrino beams of a neutrino factory and for multi-TeV lepton-antilepton collisions at a muon collider. The international Muon Ionization Cooling Experiment (MICE) has demonstrated the principle of ionization cooling, the technique by which it is proposed to reduce the phase-space volume occupied by the muon beam at such facilities. This paper documents the performance of the detectors used in MICE to measure the muon-beam parameters.

1 Introduction

Stored muon beams have been proposed as the basis of a facility capable of delivering lepton-antilepton collisions at very high energy [1, 2] and as the source of uniquely well-characterised neutrino beams [3–5]. In the majority of designs for such facilities the muons are produced from the decay of pions created when an intense proton beam strikes a target. The phase-space volume occupied by the tertiary muon beam must be reduced (cooled) before it is accelerated and subsequently injected into the storage ring. The time taken to cool the beam using techniques that are presently in use at particle accelerators (synchrotron-radiation cooling [6], laser cooling [7–9], stochastic cooling [10], and electron cooling [11]) are all long when compared with the lifetime of the muon. The use of such techniques would therefore lead to unacceptably large losses through decay. Ionization cooling [12, 13], in which a muon beam is passed through a material (the absorber), in which it loses energy, and is then re-accelerated, occurs on a timescale short compared with the muon lifetime. Ionization cooling is therefore the technique by which it is proposed cool the muon beam at a neutrino factory or muon collider. The international Muon Ionization Cooling Experiment (MICE) has provided the proof-of-principle demonstration of the ionization-cooling technique [14].

MICE was operated on the ISIS neutron and muon source at the STFC Rutherford Appleton Laboratory from 2008 to 2018. ISIS accelerates protons to 800 MeV at a repetition rate of 50 Hz. For MICE operation, a titanium target was dipped nearly once per second into the halo of the proton beam. Pions created in the interaction were captured in a quadrupole triplet (see figure 1). A conventional beam line composed of dipole, solenoid, and quadrupole magnets captured muons produced through pion decay and transported the resulting muon beam to the MICE apparatus. The momentum of the muon beam was determined by the settings of two dipole magnets. The emittance of the beam injected into the experiment adjusted using a set of adjustable tungsten and brass diffusers. The cooling cell was composed of a liquid-hydrogen or lithium-hydride absorber placed inside a focus-coil (FC) module, sandwiched between two scintillating-fibre trackers (TKU, TKD) placed in superconducting solenoids (SSU, SSD). Together, SSU, FC, and SSD formed the magnetic channel. The MICE coordinate system is such that the z-axis is coincident with the beam direction, the y-axis points vertically, and the x-axis completes a right-handed co-ordinate system.

This paper documents the performance of the instrumentation which was used to characterise fully the beam, its evolution across the magnetic channel, and to quantify the properties of the liquid-hydrogen absorber. The instrumentation was consisted of three time-of-flight detectors (TOF0, TOF1, TOF2) which are discussed in section 2, two threshold Cherenkov counters (CkovA, CkovB) discussed in section 3, a sampling calorimeter (KL) discussed in section 4, a tracking calorimeter (EMR) discussed in section 5 and the scintillating-fibre trackers (section 6). The instrumentation of the liquid-hydrogen absorber is discussed in section 7.

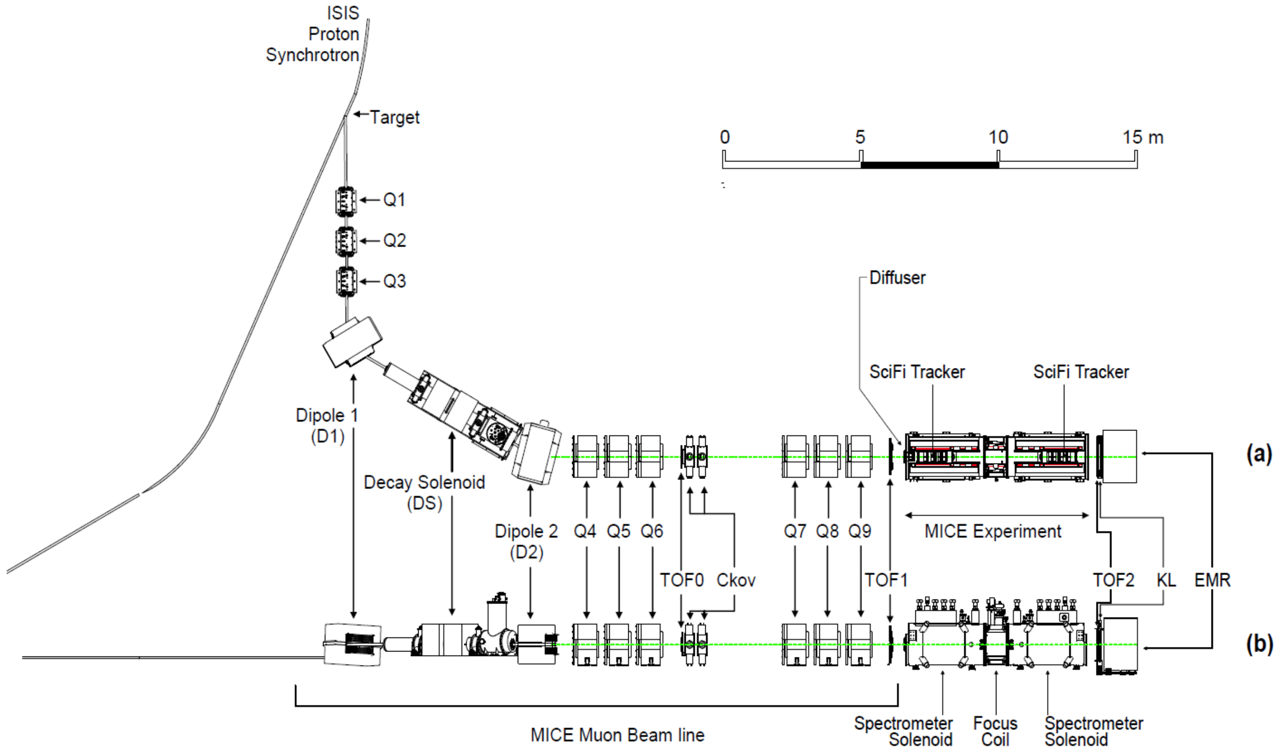

Figure 1: MICE, top (a) and side (b) views, showing the full beam line starting from the target position on the proton synchrotron with the full set of quadrupoles and dipoles (Q1 to Q9, D1, D2), the Decay Solenoid, and instrumented magnetic channel elements (including the trackers upstream and downstream of the cooling channel, placed inside superconducting solenoids) with all the other PID detectors (three TOF stations, CkovA and CkovB, KL and the EMR). The cooling channel, defined by the liquid-hydrogen absorber vessel inside the Focus Coil, is shown in figure 19.

2 Time-of-flight detectors

Three scintillator hodoscopes were used to measure the time of flight (TOF) of the particles that made up the beam, the transverse position at which the particle crossed each of the detectors, and to provide the trigger for the experiment. TOF0 and TOF1 [15–17] were placed upstream of the magnetic channel, while and TOF2 [18] was located downstream of the channel, mounted in front of the KL pre-shower detector (see figure 1). The range of particle momentum delivered to the experiment was determined by the settings of the two dipole magnets D1 and D2. At 240 MeV/c, the difference in the TOF for a muon and a pion between TOF0 and TOF1 was about 1.3 ns. The system was therefore designed to measure the TOF with a precision of 100 ps. This allowed the TOF between the first pair of TOF stations to be used to discriminate between pions, muons, and positrons contained within the beam with near 100% discrimination efficiency [19]. In addition, by assuming a particular mass for each particle, the TOF measurement was also used to infer the particle momentum. The TOF detectors operated smoothly during the running periods and were essential for all the measurements that were performed [14, 19–23].

Each TOF station was made of two planes of 1 inch thick scintillator bars oriented along the x and y directions. The bars were made of BC-404 plastic scintillator. A simple fishtail light-guide was used to attach each end of each bar to R4998 Hamamatsu fast photomultiplier tubes (PMTs). Each PMT was enclosed in an assembly that included the voltage divider chain and a 1 mm thick μ-metal shield. The shield was required to reduce the stray magnetic field within the PMT to a negligible level [17]. To increase the count-rate stability, active dividers were used. The TOF detector is illustrated in figure 2.

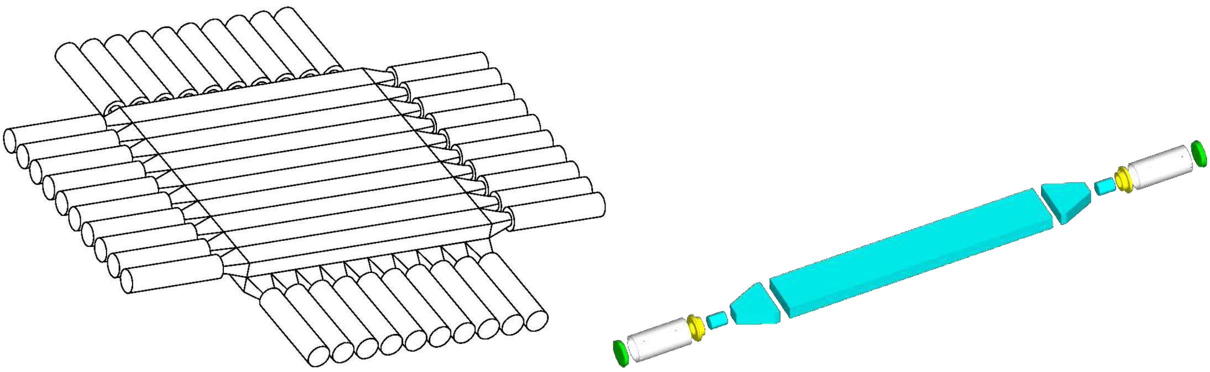

Figure 2: The structure of the time-of-flight detectors [15, 17] showing the horizontal and vertical layers of slabs (left) and an exploded view of each slab (right). The components of each slab are the central scintillator bar, two fishtail, clear plastic light-guides coupled to clear plastic matching pieces, and two PMTs. (right) on each side.

The active areas of the three hodoscopes are $40\times40\,\mathrm{cm}^2$ (TOF0), $42\times42\,\mathrm{cm}^2$ (TOF1), and $60\times60\,\mathrm{cm}^2$ (TOF2). Each of the planes in TOF0 had ten, 4 cm wide, scintillator slabs. Stations TOF1 and TOF2 were composed of 7 and 10 scintillator slabs in each plane, respectively. A passive splitter was used to take the signal from each of the PMTs to a leading-edge CAMAC Lecroy 4115 discriminator followed by a CAEN V1290 TDC for time measurement and to a CAEN V1724 FADC for pulse-height measurement. A local readout trigger was issued if the signals from the each of two PMTs on a single slab crossed a specific threshold and were coincident. TOF1 was used to trigger the readout of the experiment for most of the data taking.

Calibration

The intensity of the scintillation light produced when a particle crossed the plastic scintillator rose rapidly, subsequently decaying with a characteristic time of 1.8 ns. The scintillation light propagated from the particle-crossing point to each end of the scintillator slab. The light-travel time was dependent on the distance of the particle crossing from the PMT. The largest difference between the time of arrival of the light at the two ends of a scintillator bar occurred when a particle crossed close to one end of the bar. The light-propagation speed was determined to be approximately 13.5 cm/ns so that the maximum light-travel time differences for slabs in TOF0, TOF1, and TOF2 were approximately 3.0 ns, 3.1 ns, and 4.4 ns respectively.

The readout-trigger signal was distributed to all TDC boards and was used as the reference time. As a result of the light-propagation effect the trigger time was dependent on the position at which the particle crossed the TOF station in which the trigger was generated. As a consequence, the reference time had a bias dependent on the position of the crossing, an effect referred to as the readout-trigger signal delay. To compensate for this, the final time measurement in each station was determined as an average of the times recorded for each channel above threshold.

Further delay was introduced by the signal-transit time of each PMT and of the cable that led the signal to the readout electronics. These signal-transit times were unique for each individual readout channel and were determined in dedicated measurements. The use of a linear, leading-edge discriminator lead to a correlation between the total charge in the pulse and the time at which the discriminator fired. This correlation, referred to as the time-walk, introduced a systematic bias in the time recorded by the TDC dependent on the pulse height.

Precise determination of the TOF requires a calibration procedure that allows channel-by-channel variations

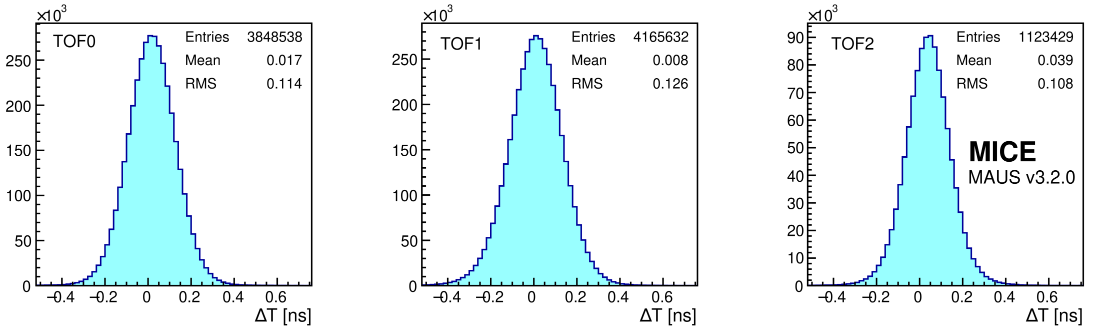

Figure 3: Slab ΔT distributions. Total width of the distribution was due to the resolution of individual pixels and due to the offsets in their ΔT distributions.

in the response of the system to be accounted for. The calibration procedure described in [24] accounted for each of the effects identified above.

Reconstruction

A particle crossing a TOF station passes through two orthogonal slabs. Signals from each PMT were corrected for time-walk, readout-trigger signal delay, and the channel-specific delays. The slab-crossing time was taken to be the average of the corrected PMT times. Two slabs were taken to have been produced by the passage of a particle if their slab-crossing times were within a 4 ns window. The two matched slabs were used to define a pixel of area given by the width of the slabs. The particle-crossing time was then determined as the average of the slab times and the approximate position of the particle crossing was refined using the PMT signals in the two orthogonal slabs.

Performance

The difference, ΔT, between the slab times for matched slabs was used to determine the intrinsic time resolution, σ_T. of the TOF system. Assuming that the intrinsic resolution is the same in each of the planes that make up a particular TOF station, the ΔT resolution, $\sigma_{\Delta T}$ will be given by $\sigma_{\Delta T} = 2\sigma_T$. Figure 3 shows the distributions of ΔT for TOF0, TOF1, and TOF2 for a representative set of data taken in 2018. The RMS width of the distributions are 114 ps, 126 ps, and 108 ps for TOF0, TOF1, and TOF2 respectively. The distributions are similar and the RMS of each distribution is consistent with the measured intrinsic resolution of approximately 60 ps [17].

Figure 4 shows an example of distribution of the measured TOF between TOF0 and TOF1. The TOF peaks characteristic of positrons, muons, and pions are clearly separated. The width of the positron peak is approximately 0.10 ns, consistent with the spread calculated from a naive quadrature addition of the timing resolution of the individual TOF stations.

3 Cherenkov Detectors

The threshold Cherenkov counters were designed primarily to provide π-μ separation for particle momentum $\gtrsim 200$ MeV/c where the precision of the time-of-flight measurment was not sufficient for conclusive particle identification. Two high-density silica aerogel Cherenkov detectors with refractive indices n=1.07 (CkovA) and n=1.12 (CkovB) were used [25]. The structure of the detectors is shown in figure 5. Light was collected in each counter by four eight-inch, UV-enhanced PMTs and recorded using CAEN V1731 FADCs (500 MS/s) [26]. The

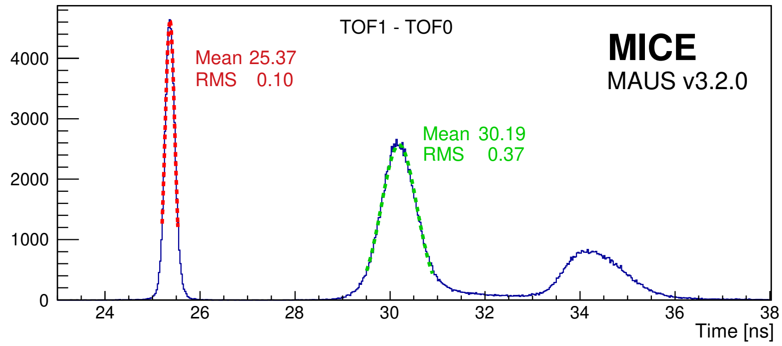

Figure 4: Time of flight between TOF0 and TOF1 after all corrections have been applied. From the left: the well separated electron, muon and pion distributions.

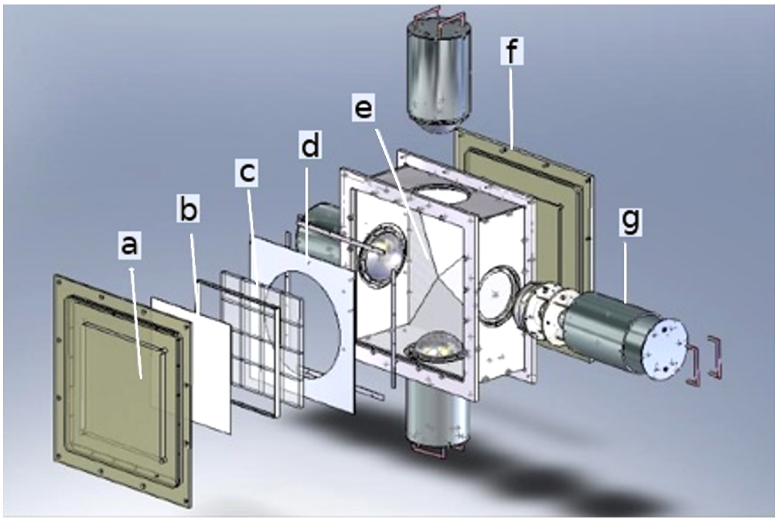

Figure 5: MICE aerogel Cherenkov counter blowup: a) entrance window, b) mirror, c) aerogel mosaic, d) acetate window, e) GORE reflector panel, f) exit window and g) eight-inch PMT in iron shield.

two detectors were placed directly one after the other in the beamline and located just after TOF0.

The refractive indices of CkovA and CkovB result in detection thresholds for muons of approximately 280 MeV/c and 210 MeV/c in CkovA and CkovB respectively. For pions the thresholds are approximately 367 MeV/c (CkovA) and 276 MeV/c (CkovB). MICE was designed to operate using beams with a central momentum between 140 MeV/c and 240 MeV/c. The thresholds of CkovA and CkovB were chosen to match this range since the TOF system was able to identify muons with high efficiency for momenta below 210 MeV/c. For momentum greater than 210 MeV/c and less than 276 MeV/c, above the maximum beam momentum, muons will produce a signal in CkovB while pions will produce no signal in either detector. Unambiguous identification of particle species using the Cherenkov exploited the measurement of momentum provided by the trackers.

3.1 Performance

Beams with a wide momentum range have been used to cover the full spectra of particles that could have been measured by the Cherenkov detectors. The asymptotic light yield (for β=v/c=1) in each counter was measured using the electron peaks, resulting in 16 ± 1 photoelectrons (NPE) in CkovA and 19 ± 1 in CkovB.

The photoelectron yields versus $\beta\gamma$ in CkovA and CkovB are displayed in figure 6, where the background NPE has not been included in the plot in order to highlight the activated part.

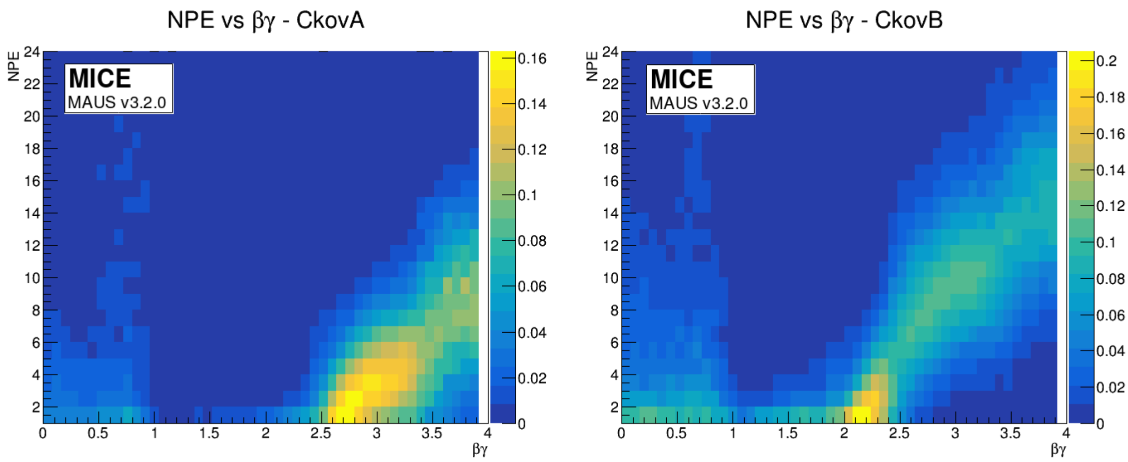

Figure 6: Photoelectron yields versus $\beta\gamma$ in CkovA and CkovB.

The refractive indices than can be calculate from the turn on point ($n = \sqrt{1 + \frac{1}{\beta_0^2\gamma_0^2}}$) are compatible with the nominal values quoted before.

4 KLOE-Light Calorimeter

4.1 Introduction

The KLOE-Light (KL) pre-shower sampling calorimeter was composed of extruded lead foils in which scintillating fibres were placed. The volume ratio of scintillator to lead was approximately 2 to 1, "lighter" than ratio used in the KLOE experiment calorimeter (1 to 1) [27].

The fibres were 1 mm diameter BICRON BCF-12, scintillating in the blue, spaced 1.35 mm from each other within a layer. The distance between two layers was 0.98 mm, one layer being shifted by half the fibre pitch with respect to the next. Scintillation light was guided from each slab into a total of six PMTs (three on each side). Iron shields were fitted to each photomultiplier to eventually mitigate against large stray fields from the magnetic channel. The signal from each PMT was sent to a shaping amplifier (SA) module, which shapes and stretches the signal in time in order to match the sampling rate of the flash ADCs (figure 7 shows the design of a single slab). A total of 7 slabs forms the whole detector, which has an active volume of 93 cm$\times$93 cm$\times$4 cm.

With its 2.5 radiation lengths, the KL was used to distinguish muons from decay electrons providing energy deposition and timing information. The detector has been used to estimate the level of pion contamination within the MICE muon beams to be around 1 % [19].

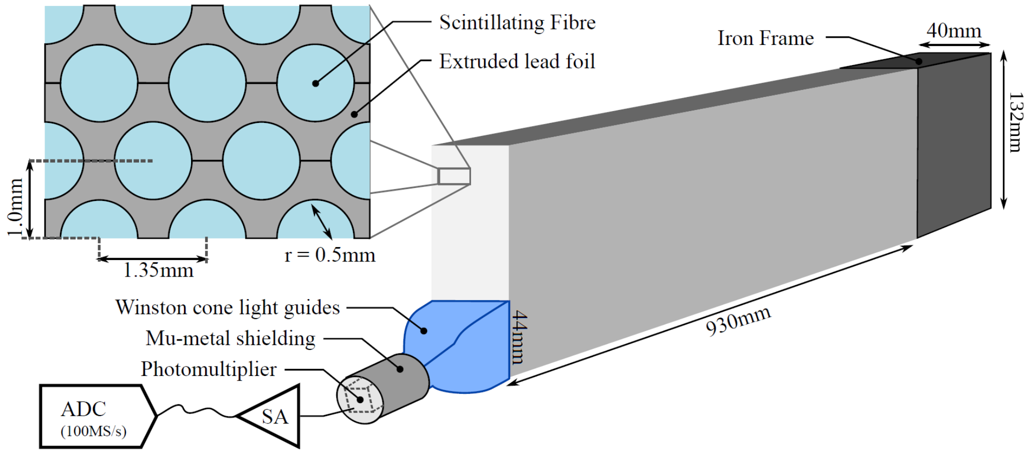

Figure 7: Single slab design of MICE KLOE-Light Calorimeter.

4.2 Performance

The study of the KL response to different particle types (muons, pions and electrons) at different momenta was based on particle identification obtained by the time-of-flight detector, as shown in the example of figure 4, by applying time cuts on the time-of-flight spectrum across the peaks of the different species. The performance is presented for beamline settings with momentum distribution centred at 140, 170, 200, 240 and 300 MeV/c. The results presented below are obtained from runs without magnetic fields in the trackers or focus coil. The KL response to muons, pions and electrons for all available momenta is presented in figure 8. Muons and pions were below the minimum ionizing particle momenta, since the energy deposition is inversely proportional to the momentum. Actually the energy deposition is approximately proportional to the sum of ADC products from all cells in KL above a given threshold. The ADC product on the other hand is the product of the left and the right side of one slab divided by the sum of left and right side: $\mathrm{ADC_{prod}} = 2 \times \mathrm{ADC_{left}} \times \mathrm{ADC_{right}}/(\mathrm{ADC_{left}} + \mathrm{ADC_{right}})$. The factor of 2 is present for normalisation. The product of two sides compensates the effect of attenuation.

The comparison of ADC products of muon, pions and electrons for a fixed momentum is presented in figure 9. For example 300 MeV/c (figure 9, bottom) muons and pions have almost the same distribution, while moving to lower energies pions have a broader distribution, experiencing hadronic interactions and loosing more energy. This pion behaviour has been used to estimate its contamination in muon samples [19].

	140 MeV/c	**170 MeV/c**	**200 MeV/c**	**240 MeV/c**	**300 MeV/c**
electrons	0.95 ± 0.02	0.95 ± 0.01	0.94 ± 0.03	0.96 ± 0.02	0.95 ± 0.02
muons	0.97 ± 0.02	0.99 ± 0.01	0.99 ± 0.01	0.99 ± 0.01	0.99 ± 0.01
pions	n/a	0.89 ± 0.03	0.95 ± 0.03	0.97 ± 0.03	0.98 ± 0.01

Table 1: Efficiency of KL for electrons, muons and pions as a function of particle momentum. The conditions required the existence of a TOF track and signal in KL above the threshold. The uncertainties are statistical.

In figure 10 we show a simulation of KL response to 300 MeV/c muons and pions and the distributions are compared with data. The simulation takes into account the distribution of the photons in the scintillator fibres, the subsequent creation of photoelectrons on photomultiplier photocathodes and the response of the photomultipliers (where gain was around 2×10^6). The agreement between data and simulation is very good.

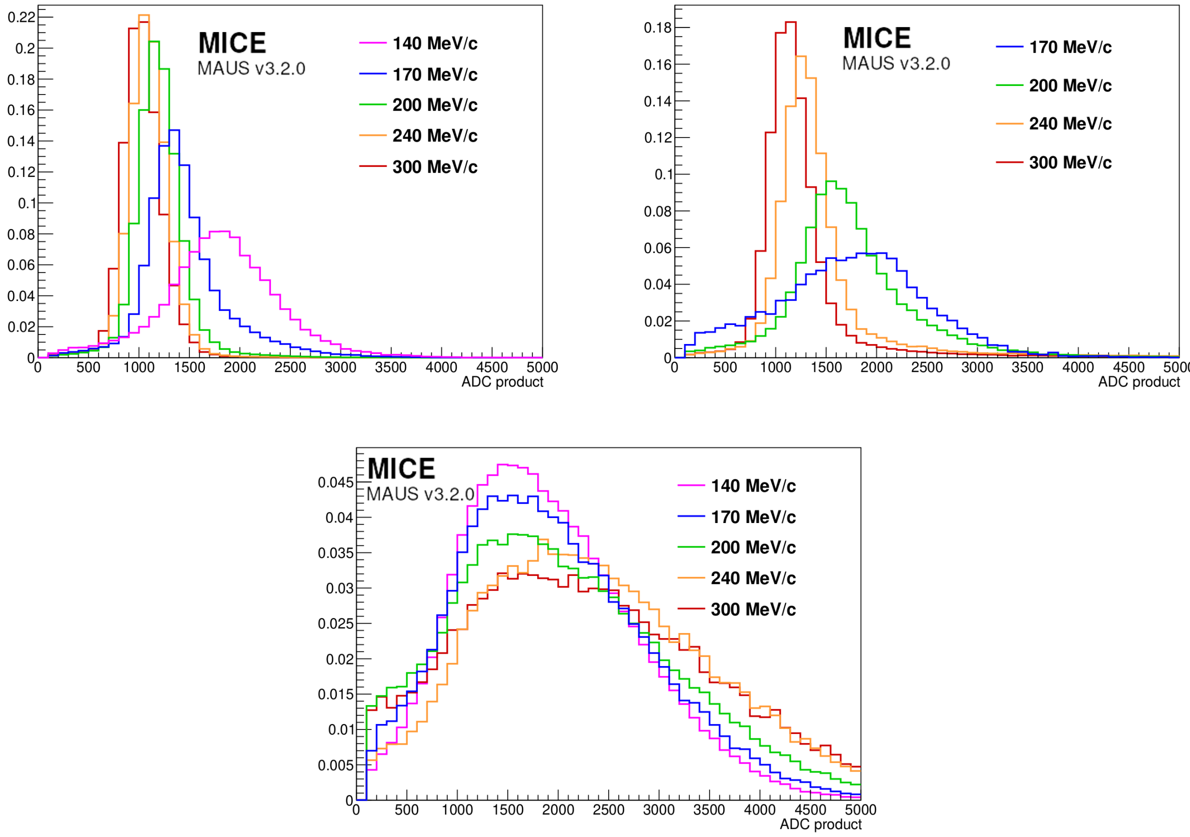

Figure 8: KL response to muons (top left), pions (top right) and electrons (bottom) for all available momenta. The charge deposited by particles in KL in arbitrary units is shown. All histograms are normalised to unity.

5 Electron Muon Ranger

5.1 Introduction

The Electron-Muon Ranger (EMR) was a fully-active scintillator detector [28]. It could be classified as a tracking-calorimeter, as its granularity allowed for track reconstruction. The EMR consisted of extruded triangular scintillator bars arranged in planes. One plane contained 59 bars and covered an area of 1.27 m^2. A cross-section of bars and their arrangement in a plane is shown in figure 11. Triangular bars were chosen rather than rectangular bars so that tracks moving parallel to the detector axis could not travel along the gaps between bars. Each plane was rotated through 90° with respect to the previous one, such that hits in a pair of neighbour planes defined a horizontal and vertical (x, y) interaction coordinate. The scintillating light was collected by a wave-length shifting (WLS) fibre glued inside the bar. At both ends, the WLS fibre was coupled to clear fibres that transported the light to a PMT. Signals produced in a plane were read out collectively on one end by a single-anode PMT (SAPMT) for an integrated charge measurement and separately on the other by multi-anode PMTs (MAPMT) for individual bar hit reconstruction. The full detector was composed of 24 X–Y modules for a total active volume of approximately 1 m^3.

Analyses were conducted to characterise the hardware of the EMR and determine whether the detector performed to specifications [29]. The clear fibres coming from the bars were shown to transmit the desired amount of light, and only four dead channels were identified. The level of crosstalk was within acceptable values for the

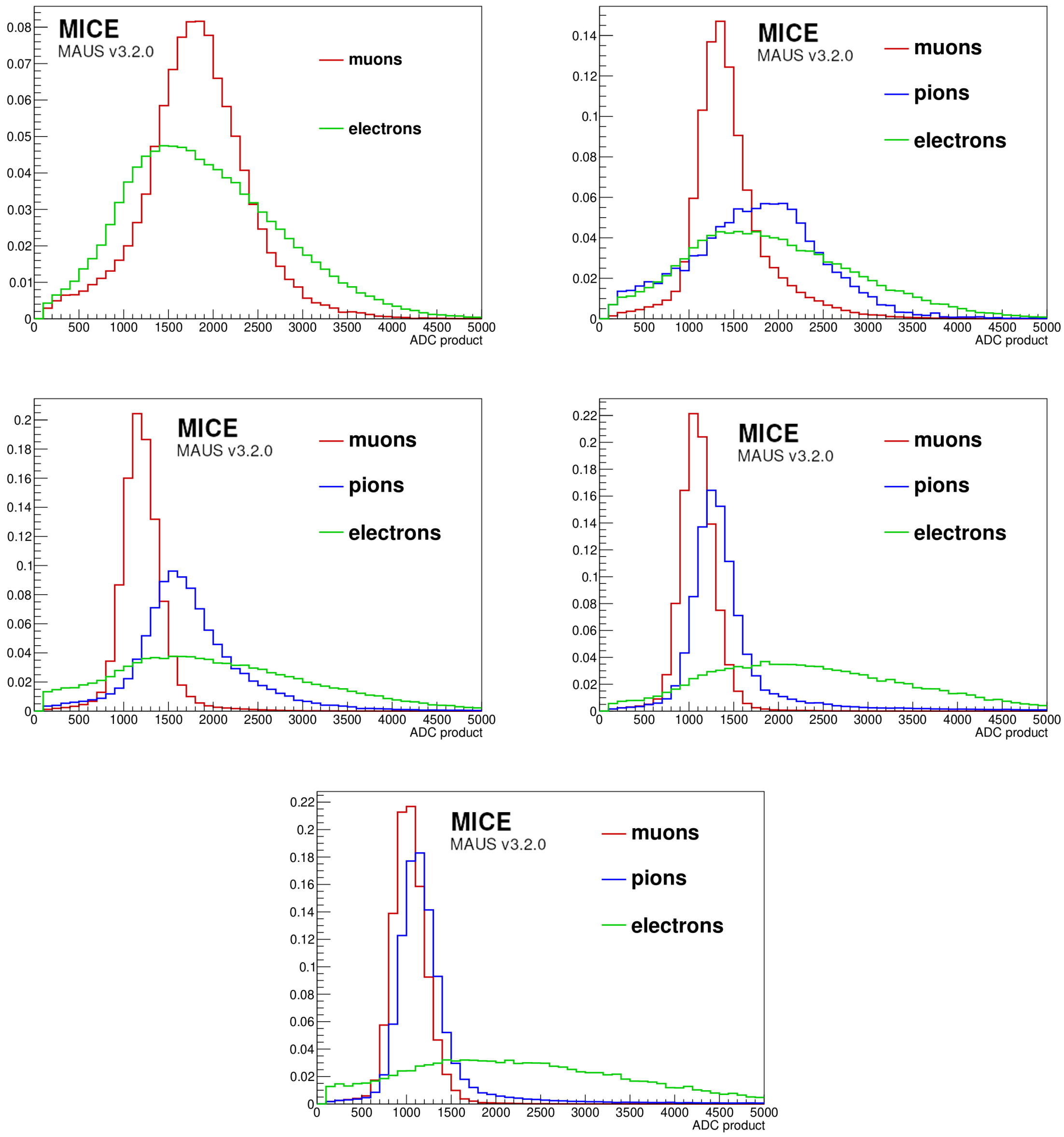

Figure 9: Comparison of ADC products of muons, pions and electrons at 140 MeV/c (top left), 170 MeV/c (top right), 200 MeV/c (middle left), 240 MeV/c (middle right) and 300 MeV/c (bottom).

type of multi-anode photomultiplier used with an average of 0.20 ± 0.03 % probability of occurrence in adjacent channels and a mean amplitude equivalent to 4.5 ± 0.1 % of the primary signal intensity. The efficiency of the signal acquisition, defined as the probability of recording a signal in a plane when a particle goes through it in beam conditions, was 99.73 ± 0.02 % [28].

The primary purpose of the EMR was to distinguish between muons and their decay products, identifying muons that have crossed the entire manetic channel. Muons and electrons exhibited distinct behaviours in the detector. A muon followed a single straight track before either stopping or exiting the scintillating volume. Electrons showered in the lead of the KL and created a broad cascade of secondary particles. Two main geometric variables, the plane density and the shower spread, were used to differentiate them. The detector was capable of identifying electrons with an efficiency of 98.6 %, providing a purity for the MICE beam that exceeds 99.8 %. The EMR also proved to be a powerful tool for the reconstruction of muon momenta in the

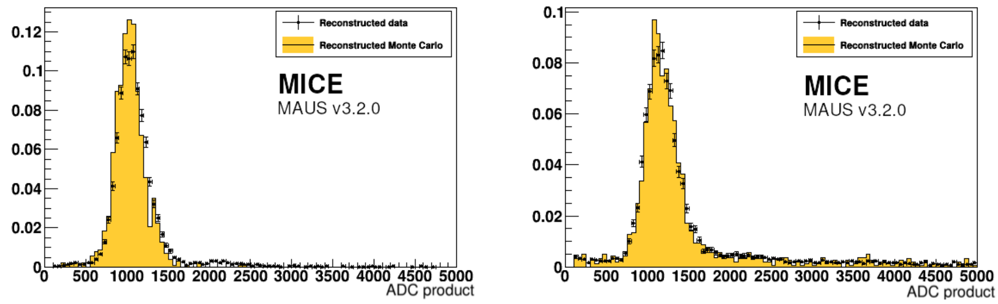

Figure 10: Comparison between data and Monte Carlo simulation of KL response to muons (left) and pions (right) at 300 MeV/c.

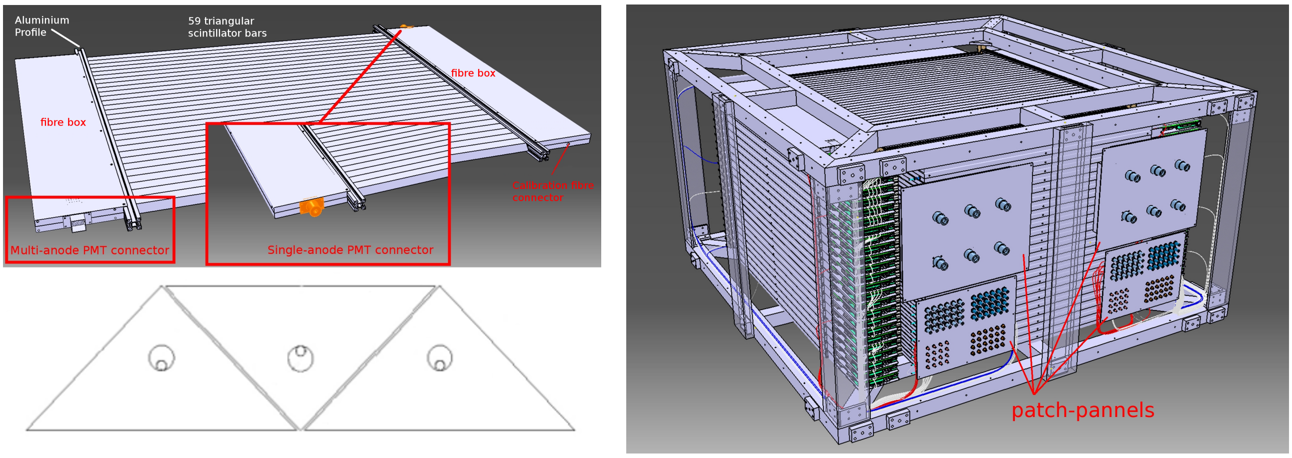

Figure 11: Drawing of one EMR plane (top left), cross section of the arrangement of 3 bars and their wavelength shifting fibres (bottom left) and drawing of the full detector and its supporting structure (right).

range 100–280 MeV/c [22].

5.2 Performance

Performance of the detector and the reconstruction algorithms were already described [22]; here the performance of the EMR detector was assessed at three levels of resolution with data acquired during different periods of data taking over the course of the experiment. The performance of the hardware itself was evaluated by analysing the characteristics of raw photomultiplier signals. The reconstruction efficiency was determined. The performance of the detector as an electron tagging device was measured.

5.2.1 Hardware efficiencies

The MICE beamline was tuned to the highest attainable momentum to maximise the transmission to the EMR detector and increase the range of particles in the detector (approximately 400 MeV/c). In this configuration the beamline produces pions and muons in comparable quantities, along with positrons. The particle species were identified by evaluating their time-of-flight between TOF1 and TOF2. Only the particles with a time-of-flight between 28 and 28.75 ns, i.e. compatible with the muon hypothesis, were included in the analysis sample.

A muon that makes it into the analysis sample has a momentum larger than 350 MeV/c right before TOF2 and was expected to cross both TOF2 and the KL without stopping and penetrate the EMR. In practice, the probability of creating an EMR event, i.e. to produce hits in the detector was $99.62 \pm 0.03\,\%$. The minor inefficiency may be attributed to pions in the muon sample that experienced hadronic interactions in the KL. If hits were produced in the detector, space points were reconstructed $98.56 \pm 0.06\,\%$ of the time.

To evaluate the efficiency of the scintillator planes, only the muons which penetrated the entire detector were used. If a signal was recorded in the most downstream plane, it was expected that at least one bar will be hit in each plane on its path and that a signal will be recorded in the single anode PMT. In $3.26 \pm 0.02\,\%$ of cases, on average, a plane traversed by a muon will not produce a signal in its MAPMT and the most probable number of bars with a hit was one, while a track was missed by an SAPMT in approximately $1.88 \pm 0.01\,\%$ of the cases.

5.2.2 Electron rejection

The main purpose of the EMR was to tag and reject the muons that have decayed in flight inside the experimental apparatus. A broad range of beamline momentum settings was used to characterise the muon selection efficiency. The particle species were characterised upstream of the detector using the time-of-flight between TOF1 and TOF2. The peaks were fitted to each setting in order to separate the muons and positrons into two templates upstream of the EMR. Particles that fell above the upper limit of the muon peak were either pions or slow muons and were rejected from this analysis.

MICE was a single-particle experiment, i.e. the signals associated with a trigger originated from a single particle traversing the detector. The multi-anode readout of each detector plane provided an estimate of the position of the particle track in the xz or the yz projection, depending on the orientation of the scintillator bars. Inside the detector muon exhibits a clean straight track while positron produced shower inside the lead of the KL and produces a disjointed and spread-out signature. Two particle identification variables based on these distinct characteristics can be defined. One is the plane density, ρ_p, defined as

$$\rho_p = \frac{N_p}{Z_p + 1}, \tag{1}$$

where N_p is the number of planes hit and Z_p the number of the most downstream plane [22]. A muon deposits energy in every plane it crosses until it stops, producing a plane density close to one. A positron shower contains photons that may produce hits deep inside the fiducial volume without leaving a trace on their path, reducing the plane density. The second variable is the normalised chi squared, $\hat{\chi}^2$, of the fitted straight track, i.e.

$$\hat{\chi}^2 = \frac{1}{N-4} \sum_{i=1}^{N} \frac{\mathrm{res}_{x,i}^2 + \mathrm{res}_{y,i}^2}{\sigma_x^2 + \sigma_y^2}, \tag{2}$$

where N is the number of space points (one per bar hit), $\mathrm{res}_{q,i}$ the residual of the space point with respect to the track in the qz projection and σ_q the uncertainty on the space point in the qz projection, $q = x,\ y$ [30]. The number of degrees of freedom is $N - 4$, as a three-dimensional straight track has four parameters. This quantity represents the transverse spread of the particle's signature in the EMR. A muon follows a single track and is expected to have a $\hat{\chi}^2$ close to one, while an electron shower is expected to produce a larger value. The two discriminating variables can be combined to form a statistical test on the particle hypothesis. Dense and narrow events will be tagged as muons while non-continuous and wide electron showers will not. The quality of a test statistic may be characterised in terms of the loss, α, the fraction the muon sample that is rejected, and the contamination, β, the fraction of the electron sample that is selected.

The downstream tracker allows for the reconstruction of particle momentum before entering the EMR. To assess the influence of momentum on contamination and loss, their values were calculated, because of the resolution, for 10 MeV/c bins in the range 100–300 MeV/c. The test statistic calculated in each bin was based on the optimal set of cuts optimised for the whole sample, i.e. $\rho^* = 86.131\,\%$ and $\hat{\chi}^{2*} = 14.229$. Figure 12 shows the loss, α, and the contamination, β, as a function of the momentum measured in TKD. It shows that, at low momentum, the apparent muon loss increases. This is due both to an increase in decay probability between TOF2 and the EMR, and a decrease in the number of muons that cross the KL to reach the EMR.

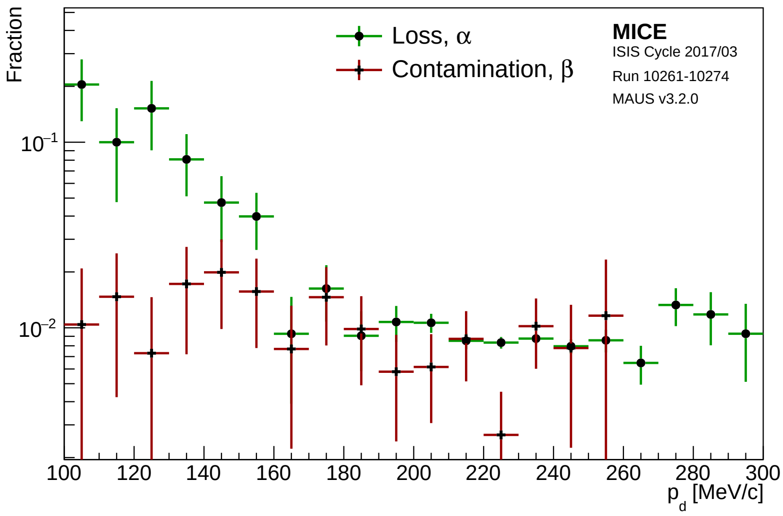

Figure 12: Percentage of electron contamination, β, and muon loss, α, for different ranges of momentum measured in the downstream tracker, p_d. The error bars are based on the statistical uncertainty in a bin.

250 # 6 Tracking

Particle were tracked across more than 15 m of instrumented beamline and magnetic channel, from the first TOF station to the EMR. High resolution particle tracking was provided by the two trackers (section 6.1), while the combined use of TOF stations and trackers was used for a precise alignment of the latter inside the superconducting magnets (section 6.2).

255 ## 6.1 Trackers

6.1.1 Introduction

MICE was equipped with two identical, high precision scintillating-fibre trackers, described in [31]. One tracker, TKU, was upstream of the cooling cell, the other, TKD, was downstream, as shown in figure 1. Each tracker was placed in a superconducting solenoid (SSU and SSD, upstream and downstream respectively) designed to provide a uniform magnetic field over the tracking volume.

The trackers were 110 cm in length and 30 cm in diameter for the active region (see figure 13). There were five stations per tracker (labelled 1 to 5, with station 1 being closest to the cooling cell) held in position using a carbon-fibre space-frame. Adjacent stations were separated by different distances of 20–35 cm, ensuring that the azimuthal rotation of track position from one station to the next differs; this difference is important in resolving ambiguities at the pattern-recognition stage. Each tracker was instrumented with an internal LED calibration system and four 3-axis Hall probes to monitor the field.

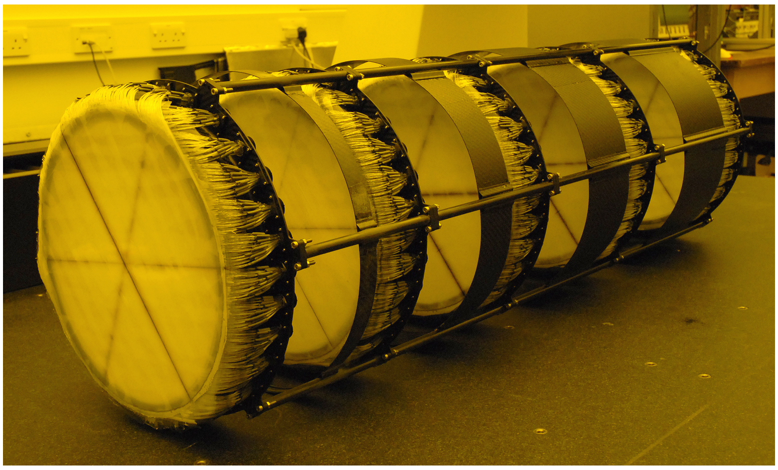

Figure 13: Photograph of one of the MICE trackers, showing the five stations and the three doublet planes of scintillating fibres, each plane at 120° angles to the next (the central fibres of plane can be seen as darker lines traversing the station). Bundles of seven 350 μm fibres were grouped together, to be read out by 1 mm light guides.

The tracker stations consisted of three doublet layers of 350 μm scintillating fibres, these layers were arranged such that each was at an angle of 120° with respect to the next. This arrangement ensured that there were no inactive regions between adjacent fibres. Bundles of seven fibres were grouped into a single readout channel (this reduced the number of readout channels, while maintaining a sufficient spatial resolution). The trackers had a spatial resolution per doublet layer of 470 μm and measured light yield of approximately 10 photo-electron [31].

The light from the seven scintillating fibres passed into a single clear fibre, which took it to a visible light photon counter (VLPC) which operated at 9 k. The signals from the VLPCs were digitised using electronics developed by the D0 collaboration [32].

6.1.2 Performance and Reconstruction

Each of the 15 tracker planes (3 per station) consisted of 214 channels. Particle signals were recorded by the tracker electronics and calibrated channel by channel then converted into signal NPE. The NPE value combined with the channel number formed a "digit", the first step in tracker reconstruction. Digit profiles were useful in identifying and rectifying or removing hot or dead channels in the planes and ensuring the accuracy of calibration. A centrally peaked spectrum could be expected in each plane in absence of dead channels and minimal electronics noise; this was not an essential requirement, since a space point in a track was made out of two or three planes, having a redundancy built in. Hence a significant fraction of individual channels can be lost without a knock on drop in efficiency. The clustering algorithm looped over every combination of pairs of digits in a single event and combined any that occur in neighbouring channels. In the case of a multi-digit cluster, the unweighted average channel value was used to define the plane coordinate and the NPE was summed.

For each station the constituent planes were searched for clusters that can be used to form a spacepoint. Spacepoints were constructed from clusters from all three planes (a triplet spacepoint) or from any two out of the three planes (a doublet spacepoint) [33].

6.1.2.1 Noise

The scintillating fibre trackers operated by registering digits above a given NPE threshold within each fibre plane. Fibres were collected into channels as ganged bundles of 7 for each channel, with digits registered per channel instead of per fibre. From a coincidence of digit events in 2 or 3 oblique channels (fibres in different planes), a spacepoint was reconstructed, from which track reconstruction was initiated. We considered noise in the tracker to be those digits registered not from the passage of a beam particle, but instead from other sources, for instance, dark current from thermal electron emission in the VLPCs. To isolate noise from signal during beam-on data collection, a strict cut can be made requiring that only events with one fitted track and 5 spacepoints per tracker were selected, with all 5 spacepoints included in the fitted track. All digits corresponding to the track were then removed from the total set of digits for that event, and the remainder were considered noise digits. An in-situ approximation of active channels for the current data taking period was made, assuming all channels without at least one registered digit in the selected data taking run were inactive. The average noise rate per channel per event was then calculated as the total number of event digits above the considered NPE threshold in each tracker, divided by both the number of active channel and the number of events satisfying the above selection criteria. This gave a value of 0.18 % upstream and 0.06 % downstream for events above 2 NPE.

6.1.2.2 Track Finding Efficiency

Data were analysed in order to determine the track and spacepoint finding efficiency of the detectors during running conditions. A time-of-flight cut was used to ensure that each measured track had a time-of-flight consistent with a muon throughout the entire experimental apparatus. A hit was therefore required in each of the TOF1 and TOF2 detectors, which ensured that the particle must have been successfully transmitted through the magnetic channel, crossing both tracking detectors. These requirements ensured that there was a better then 99.9 % probability that a particle have traversed a tracking detector. The number of events missing a track was therefore measured and used to estimate the efficiency of the detector. The results of the efficiency analysis are tabulated in table 2 for a range of momentum and nominal emittance. A track-finding efficiency of 98.70 % was calculated for the upstream and 98.93 % for the downstream tracker, averaged over field and beam conditions. In addiction, assuming a track was found, the probability of successfully finding each spacepoint is summarised in table 3. The overall efficiency of both trackers was high to do not present any significant systematic uncertainties in the analysis, however it was lower than the ideal expectation, 99.9 % efficiency, due to the presence of dead channels.

Momentum	**Nominal Emittance**	**Upstream Tracks Found**	**Downstream Tracks Found**
200 MeV/c	6 mm	99.42 %	96.07 %
200 MeV/c	3 mm	98.38 %	99.19 %
140 MeV/c	6 mm	98.37 %	99.16 %
140 MeV/c	10 mm	98.47 %	98.93 %
Averaged		98.70 %	98.21 %

Table 2: The track finding efficiency for the upstream and downstream trackers for 140 MeV/c and 200 MeV/c beams, and for 3, 6 and 10 mm nominal emittances.

Momentum	Nominal Emittance	Upstream Spacepoints Found	Downstream Spacepoints Found
200 MeV/c	6 mm	99.41 %	94.63 %
200 MeV/c	3 mm	98.04 %	97.41 %
140 MeV/c	6 mm	97.99 %	99.16 %
140 MeV/c	10 mm	98.07 %	97.44 %
Averaged		98.44 %	97.01 %

Table 3: The spacepoint finding efficiency, assuming the presence of a track, for the upstream and downstream trackers for 140 MeV/c and 200 MeV/c beams, and for 3, 6 and 10 mm nominal emittances.

6.1.2.3 Track Fit Performance

Monte Carlo simulation was used with realistic field and beam conditions to estimate the reconstruction performance. A beam centred at 140 MeV/c with 10 mm nominal emittance, representing a typical data set, was used for the study of emittance evolution. Results are presented in figure 14 for the upstream tracker and figure 15 for the downstream tracker, showing the predicted reconstruction bias and resolution for the total and the longitudinal component of the momentum.

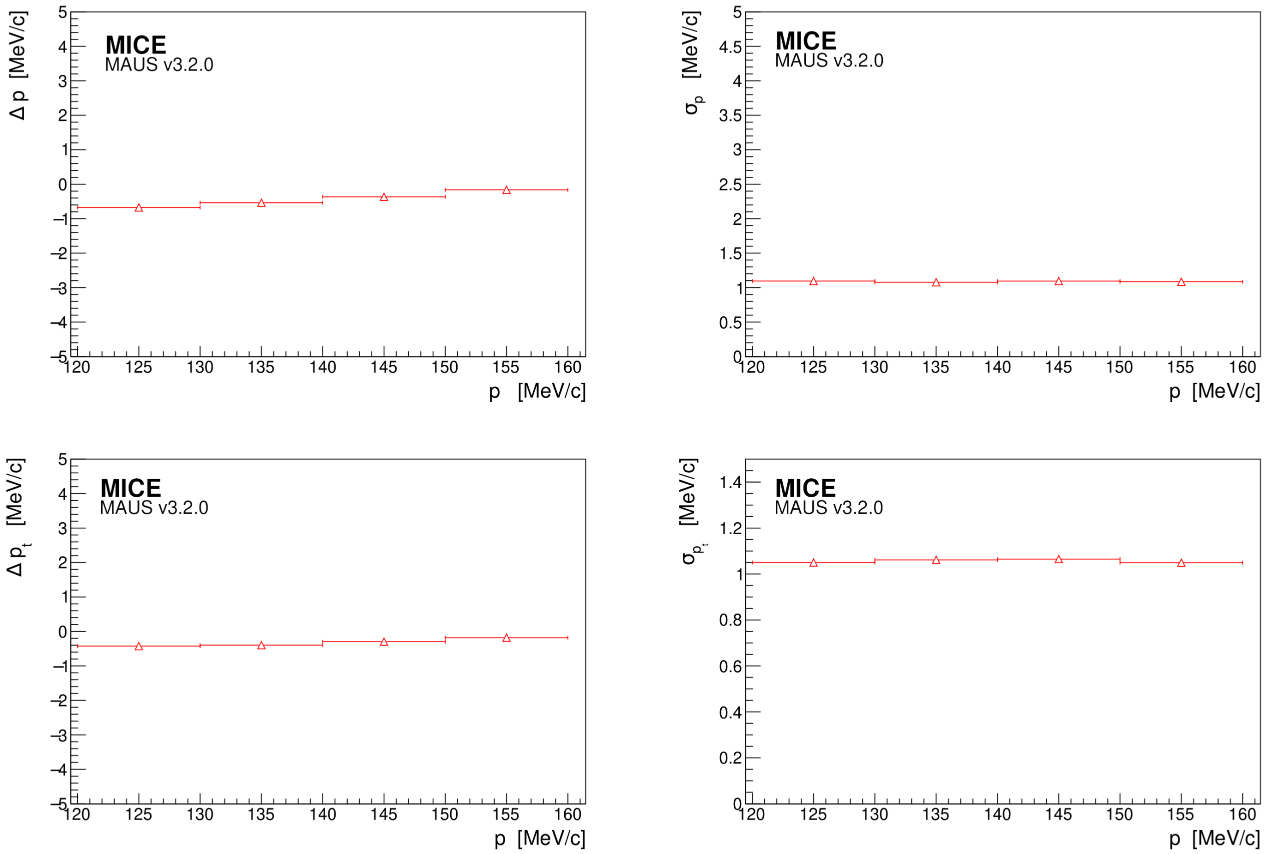

Figure 14: Predicted momentum reconstruction bias (left) and resolution (right) for the total momentum (top) and transverse momentum component (bottom) in the upstream tracker.

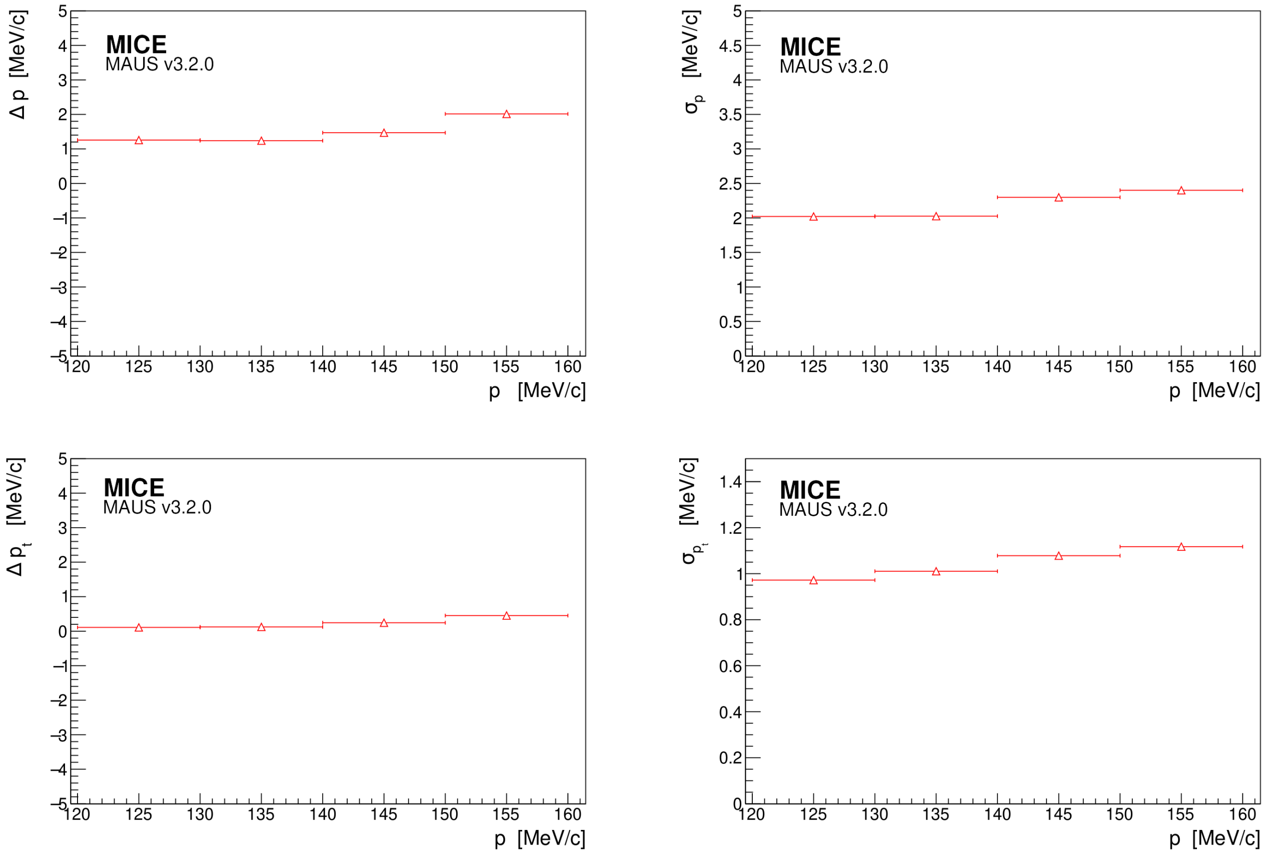

Figure 15: Predicted momentum reconstruction bias (left) and resolution (right) for the total momentum (top) and transverse momentum component (bottom) in the downstream tracker.

6.1.3 Efficiency evolution

The efficiency of the tracker was processed over the lifetime of its use during the data taking. The analysis used in section 6.1.2.2 was repeated and automated for runs starting in 2015. The selection of events used in the analysis included two more constraints:

1. A spacepoint was required to be reconstructed within the tracker volume using a radial cut; and
2. Only a single spacepoint was reconstructed in each of the stations.

The evolution of track finding efficiency in the upstream and downstream trackers for tracks in absence and presence of magnetic field in the magnetic channel (respectively "straight" and "helical") is shown in figure 16, showing efficiencies generally above 99.0 %. The variation in efficiency over time was primary due the loss of VLPC channels from moisture infiltration into the system and then partial recovery with drying.

6.2 Beam-based Detector Alignment

6.2.1 Introduction

A beam-based alignment algorithm was developed to improve the resolution on the position of the scintillating-fibre trackers located inside the bores of superconducting magnets. This method was used to determine the azimuthal orientation of the trackers with a resolution of 6 mrad/$\sqrt{N}$ and their position with a resolution of

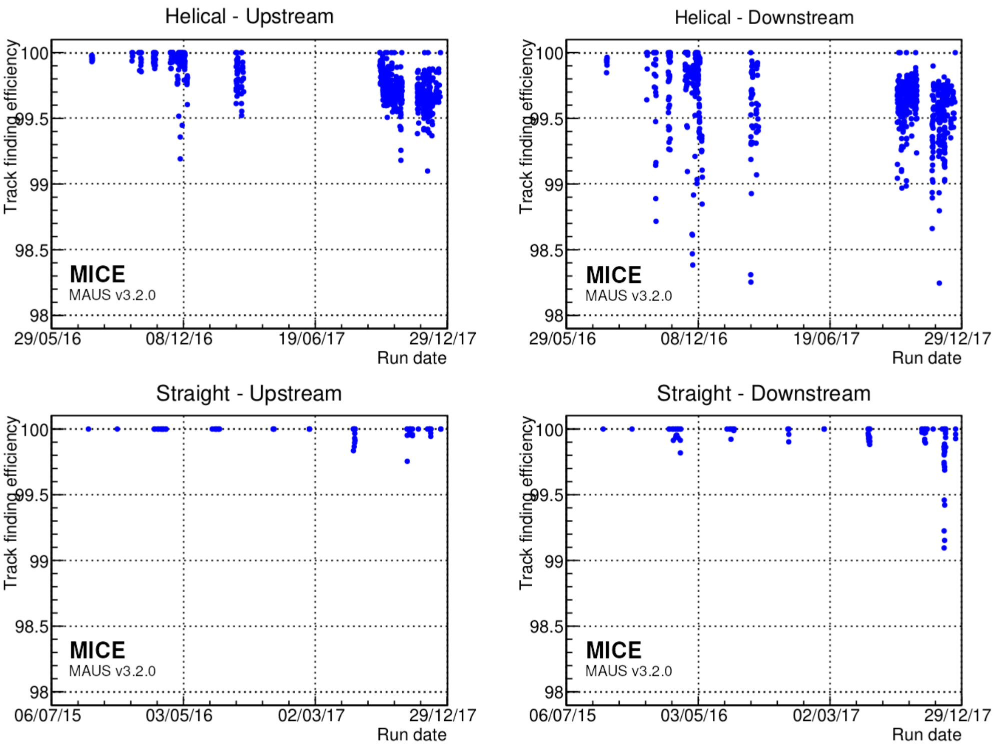

Figure 16: Evolution of the straight and helical track finding efficiency over time for the upstream (left) and downstream (right) trackers during the key periods of data taking since 2015.

20 mm/$\sqrt{N}$, where N is the number of selected tracks [34], while we do not have resolution on the position along the beam axis or rotation about it.

The starting point for the beam-based alignment was the geometrical survey of the detectors in the MICE hall which was performed using laser telemetry. Only the trackers, nested in the superconducting solenoids, could not be accessed, so their position was inferred with respect to the flanges of the solenoids and the beam-based alignment was used to verify their alignment.

6.2.2 Analysis method

The position of each tracker in global coordinates was entirely defined by the location of its centre and a set of three angles. Since the position of each tracker along the beamline was known to great accuracy from the survey and the rotation about z has a negligible influence on the alignment, only 4 constants had to be determined for each tracker.

The surveyed location of the TOFs was used as the reference for the tracker alignment. The line that joins the centre of TOF1 with the centre of TOF2 was chosen to be the reference axis. A deviation from this axis was considered as a misalignment of the trackers. Multiple scattering in the beamline would not allow to calculate the alignment on single-particle basis. For example, figure 17 shows the path of a single particle that scatters in the absorber module of MICE. The mean residual angles and positions of the trackers with respect to the TOF1–TOF2 axis were evaluated to allow the correction factors to be determined.

Each TOF provided a single space point in the global coordinate system. This position was assumed to be the true position with a with a 2–3 cm uncertainty due to the limited granularity of the detector. Trackers sampled the particle track in five different stations and this allowed for the reconstruction of a straight track without any assumption made on the prior position of the tracker. In global coordinates, on average, the track reconstructed

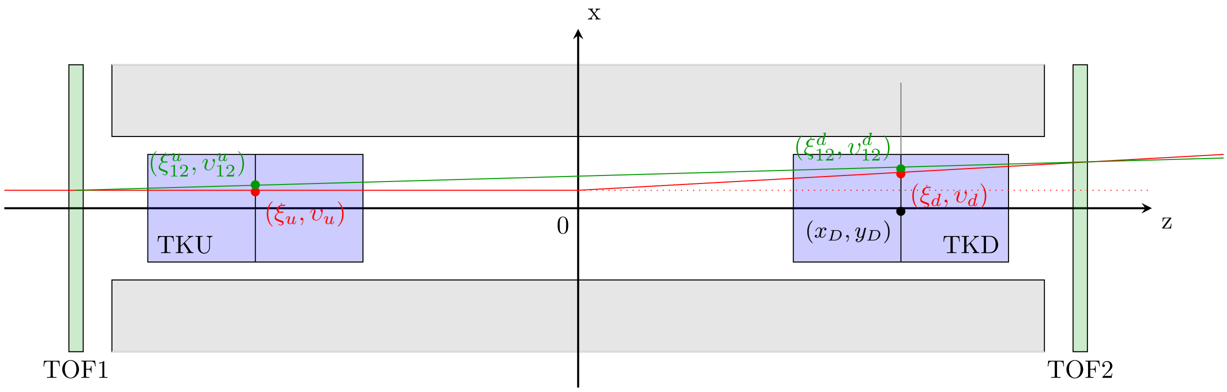

Figure 17: True path of a single particle track (red) and its path as reconstructed from the time-of-flight system (green). The position of the track at the tracker centres is represented by markers.

between TOF1 and TOF2 should agree with the track reconstructed in either tracker, i.e. the mean residuals should be zero. Applying this reasoning to the unknown offset and angles leads to a system of equations for the four unknown constants [34]. The measurement of four residual distributions per tracker yields the alignment constants. The main source of bias was the scattering in the material between TOF1 and TOF2. If the beam was not perfectly centred, particles preferentially scraped out on one side of the magnet bore, anisotropically truncating the tail of the residual distribution. A fiducial cut is applied to the upstream sample in order to remove this effect.

Data were recorded with the superconducting magnets of the experiment turned off. High momentum beams were used to reduce the RMS scattering angle and maximise transmission. Each data set was processed independently. Figure 18 shows the alignment parameters measured for each run during a specific data taking period. The measurements are in good agreement with one another and showed no significant discrepancy: an agreement between the independent fits guaranteed an unbiased measurement of the alignment constants. The constant fit χ^2/ndf was close to unity for each fit, which indicated that there were no significant additional source of uncertainty. The optimal parameters are summarised in table 4.

	x [mm]	**y [mm]**	α **[mrad]**	β **[mrad]**
TKU	-0.032 ± 0.094	-1.538 ± 0.095	3.382 ± 0.030	0.412 ± 0.029
TKD	-2.958 ± 0.095	2.921 ± 0.096	-0.036 ± 0.030	1.333 ± 0.030

Table 4: Summary table of the optimal alignment constants measured in the high-momentum straight-track data acquired during part of 2017 data taking.

7 Liquid-Hydrogen Absorber

7.1 Introduction

The absorber vessel consist of a cylindrical aluminium body sealed with two thin aluminium end windows, as shown in figure 19. The absorber vessel has a volume of 22 l of liquid with body dimensions with an inner diameter of 300 mm and a length between its end flanges of 230 mm. The length along the central axis between the two domes of the thin aluminium end windows was 350 mm [35].

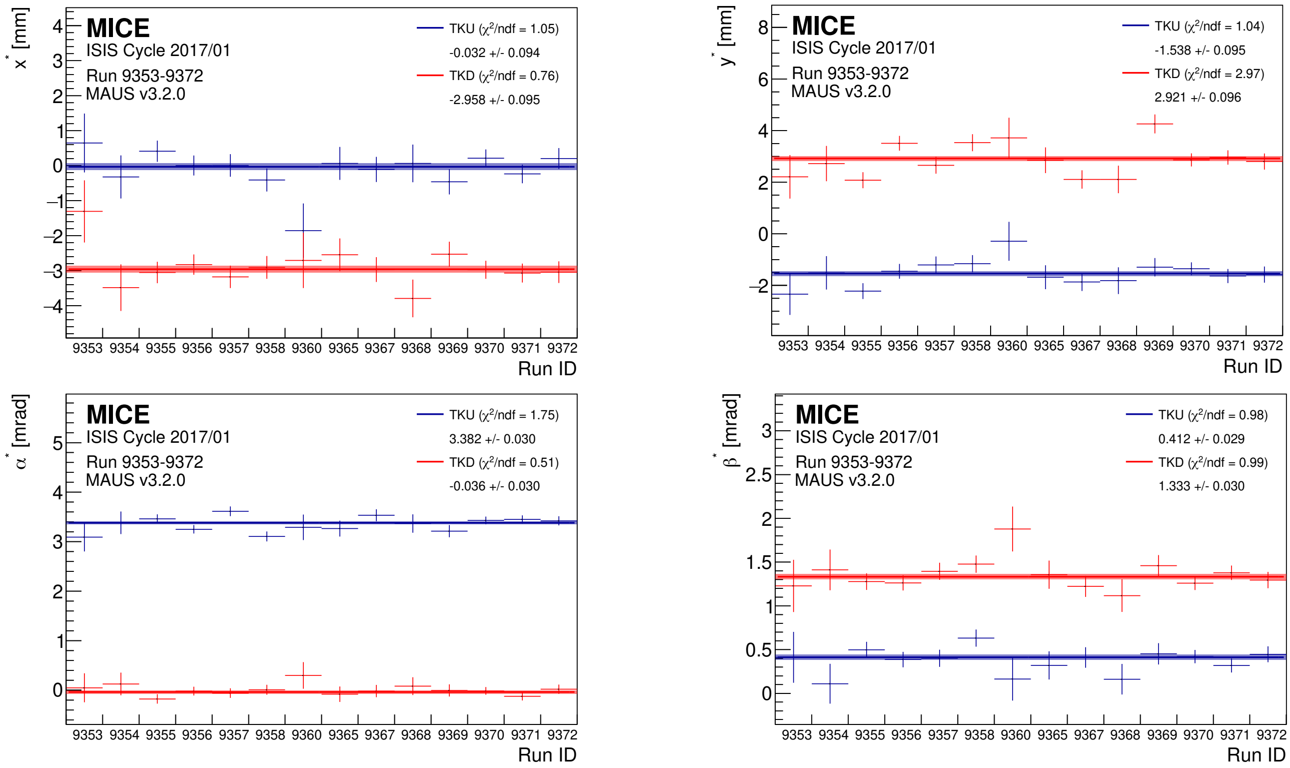

Figure 18: Consistency of the alignment algorithm across runs acquired during the 2017/01 ISIS user cycle.

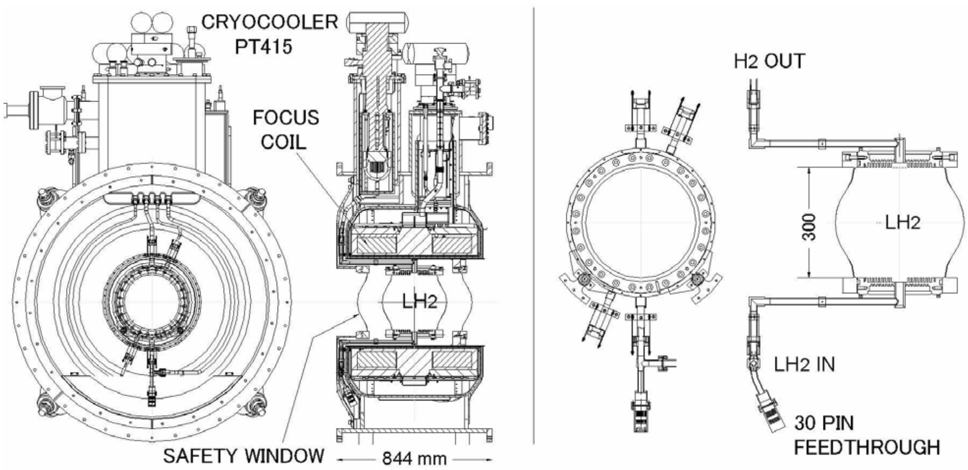

Figure 19: Left panel: Drawing of the absorber/focus-coil (AFC) module showing the principal components. Right panel: detail of the liquid-hydrogen absorber vessel.

7.2 Systematic studies

7.2.1 Variation of the density of liquid-hydrogen due to varying temperature and pressure

The energy lost by a muon travelling through the liquid-hydrogen absorber depends on the path length the muon travelled through and on the density of the liquid-hydrogen. The density of liquid-hydrogen is a function of temperature and pressure. The temperature of the vessel was recorded by eight LakeShore Cernox 1050 SD sensors with a resolution of 0.1 K. Four of the sensors were used solely as temperature sensors, while the other four were used also as level sensors to ensure the liquid-hydrogen reached the top of the vessel. They were arranged in pairs with two mechanically clamped at the top of the vessel, two at a rotation of 45°, a further two at a further rotation of 90° and a final two at a further rotation of 45° to be at the bottom of the vessel.

Cooldown and liquefaction were completed slowly over eight days at a pressure of 1.15 Bar after which the vessel's pressure was lowered to 1.085 Bar [35]. The vessel then remained in this steady-state equilibrium until the venting process began. During this process the cryocooler was switched off and the heaters were switched on, delivering a nominal power of 50 Watt to the absorber vessel. This resulted in an increase in pressure and temperature until the temperature stabilised at the boiling point. A rapid increase in temperature was observed once all the liquid-hydrogen had boiled off.

The sensors have a typical accuracy of ± 9 mK and a long-term stability of ± 12 mK at 20 K. The magnetic-field dependent temperature error at 2.5 T is 0.04 %, ΔT/T, equivalent to ± 8 mK at 20 K [36][37]. These are the quoted uncertainties given by the manufacturer of the sensors. The importance of magnetic fields on temperature measurements is that they cause reversible calibration shifts: when the magnetic field is removed, the sensors return to their original calibration.

To reduce the uncertainty in the liquid-hydrogen density a calibration procedure was devised using the boiling point: the corrected temperature reading was found by applying a cut-off correction, a magnetic field correction based on the focus coil current and polarity, a correction for the non-linearity of the sensors, and a boiling point scaling factor [38].

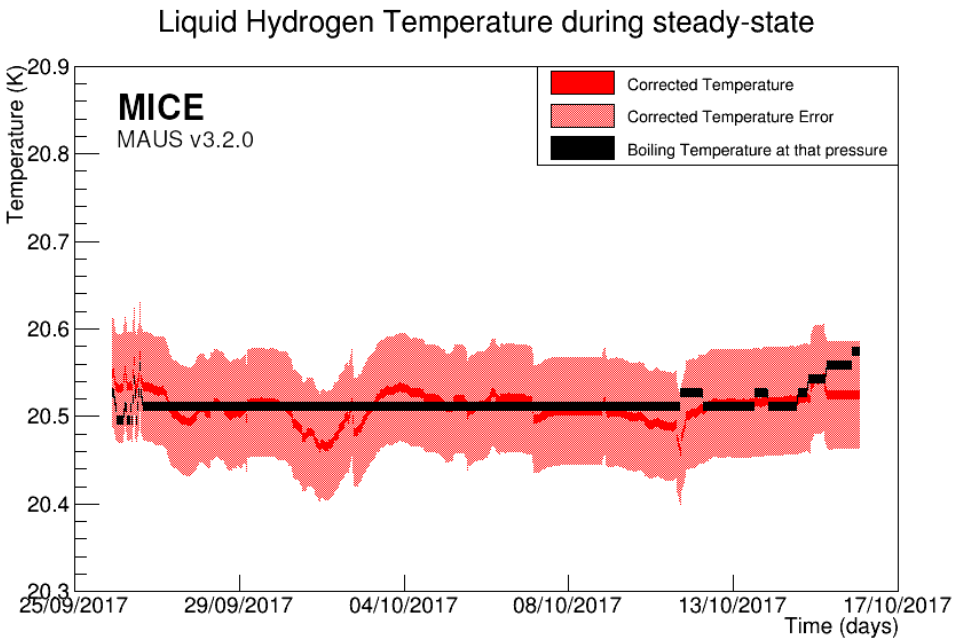

Figure 20: Average LH2 temperature recorded by the sensors during the steady-state period. After applying all the correction factors the temperature remains at or close to the boiling point temperature.

The boiling point of hydrogen at 1.085 Bar is 20.511 K. There are however a number of uncertainties. The sensors have a total uncertainty of 17 mK (9 mK accuracy, 12 mK stability, 8 mK magnetic). The deviation from the non-linearity of the sensors adds an average error of 0.03 K. The temperature scaling and magnet current correction factors also have an associated error as they are based on the 0.1K resolution. For example, a calibrated sensor at boiling temperature and 1.505 Bar should read 21.692 K, but can only read 21.65 K (21.6 K cut-off plus 0.05 cut-off correction) i.e. it is off by 0.042 K. The pressure sensors have an uncertainty of ± 5 mBar which equates to ± 0.016 K during steady state. The pressure uncertainty (± 5 mBar) adds another uncertainty to the temperature calibration constants of $\pm\,0.014$ K. Collectively, all these uncertainties add up to 0.2 K for each sensor.

For our steady state condition the liquid-hydrogen was close to the boiling temperature of liquid parahydrogen [38] with a density of 70.53 kg/m^3. The average temperature of the eight sensors during steady-state was (20.51 ± 0.07) K at 1.085 Bar (figure 20) and allows us to determine the uncertainty in the density as 0.08 kg/m^3.

7.2.2 Contraction of the absorber vessel due to cooling

The aluminium absorber vessel was cooled from room temperature to the operating temperature of the experiment (20.51 K), which resulted in the vessel contracting. The linear contraction of Al-6061 as it is cooled from 293 K is given by:

$$\alpha = -4.1277 \times 10^{-3}\mathrm{T} - 3.0389 \times 10^{-6}\mathrm{T}^2 + 8.7696 \times 10^{-8}\mathrm{T}^3 - 9.9821 \times 10^{-11}\mathrm{T}^4 \tag{3}$$

where T is the operating temperature [39]. The equation is a line of best fit of data collated by NIST (National Institute of Standards and Technology) and has an associated curve fit error of 4 %. At the MICE operating temperature, this corresponds to a linear contraction of the vessel along each plane of 0.415 %, resulting in a warm bore length (350 mm) contraction of (1.45 ± 0.05) mm. The vessel was held suspended in place, meaning the vessel was free to contract within the warm bore of the focus coil along each plane without restriction.

7.2.3 Deflection of absorber vessel windows due to internal pressure

To minimise energy loss and Coulomb scattering by the absorber vessel, the windows were kept as thin as possible, still being able to handle any internal pressure they are subjected to. It was necessary for the liquid-hydrogen circuit to be pressurised above atmospheric pressure to prevent air ingress [35][40]. The vessel must also be capable of handling up to 1.5 Bar, the relief valve set pressure.

These pressures resulted in a deflection of the absorber windows and were modelled using ANSYS [41]. The uncertainty in the model's window deflection was 20 %. It showed a linear expansion of the window deflection with pressure up to 2 Bar when the windows begin to yield. The pressure sensors were accurate to $\pm\,5$ mBar (0.25 % of 2 Bar). At (1085 ± 5) mBar, the typical MICE operating pressure, this corresponded to a deflection of (0.5374 ± 0.1076) mm (model uncertainty) $\pm\,0.0022$ mm (sensor uncertainty) at the centre of the absorber window.

7.2.4 Variation of the absorber vessel window thicknesses

The amount of energy loss and cooling experienced by a muon passing through the absorber depends on the amount of aluminium and liquid-hydrogen traversed. There were four windows, two absorber wall windows of the vessel and two safety windows.

At the centre of the absorber, the total amount of aluminium the muon beam passes through was (785 ± 13) μm, a variance of 1.68 %. However, as the windows were thin, the effects on energy loss were negligible. A 200 MeV/c muon passing along the central axis of an empty absorber loses 0.345 MeV, which introduces a 0.006 MeV uncertainty on energy loss.

7.2.5 Total Systematic Uncertainty on Energy Loss

In total there are three main contributions to the systematic uncertainty of the liquid-hydrogen absorber on energy loss. The contraction of the absorber and deflection of the absorber window due to internal pressure reduces the central warm bore length by (0.4 ± 0.2) mm.

The combined absorber window's thickness variation at the centre of the absorber is 13 μm. The average temperature during the steady state period of the experiment when the pressure remained constant at (1085 ± 5) mBar is (20.51 ± 0.07) K corresponding to a liquid-hydrogen density of (70.53 ± 0.08) kg/m^3.

The energy loss is momentum dependent. Tables 5 and 6 show the energy loss at various momenta for aluminium and for various densities of liquid-hydrogen, respectively [42][43][44][45]. 277 MeV/c and 344 MeV/c are the minimum ionization momenta of aluminium and liquid-hydrogen, respectively.

Table 5: Energy Loss for aluminium (Al-6061) at various nominal muon momenta with a density of 2.699 g/cm^3.

Momentum	**100 MeV/c**	**140 MeV/c**	**200 MeV/c**	**277 MeV/c**
Mass Stopping Power [MeVg^{-1}cm^2]	1.798	1.688	1.630	1.615
Stopping Power [MeVcm^{-1}]	4.8528	4.556	4.3994	4.3589

During the MICE data taking, muon beam of momentum 140, 170, 200 and 240 MeV/c were used. The energy loss and its uncertainty were calculated. The calculation used a central bore length of (349.6 ± 0.2) mm, a total window thickness of (0.785 ± 0.013) mm and a liquid-hydrogen density of (70.53 ± 0.08) kg/m^3 for a particle travelling straight through the centre of the absorber.

For a 140 MeV/c muon particle this corresponds to an energy loss of (10.88 ± 0.02) MeV, while for a 200 MeV/c muon particle this corresponds to an energy loss of (10.44 ± 0.02) MeV. In terms of energy loss, the systematic error is 0.2 %. This is for a particle travelling along the central axis of the absorber. A muon travelling through the absorber in the presence of a magnetic field would take a different path and thus would traverse a different length of aluminium and liquid-hydrogen.

8 Conclusions

A complete set of particle detectors has permitted the full characterisation and study of the evolution of the phase space of a muon beam through a section of a cooling channel, leading to the first measurement of ioniza-

Table 6: Energy loss for liquid-hydrogen at various densities (0.0703 to 0.0708 g/cm^3) and various muons momenta.

Momentum	**100 MeV/c**	**140 MeV/c**	**200 MeV/c**	**344 MeV/c**
Mass Stopping Power [MeVg^{-1}cm^2]	4.568	4.267	4.104	4.034
Stopping Power [MeVcm^{-1}] (at ρ=0.0703)	0.3211	0.29997	0.2885	0.28359
Stopping Power [MeVcm^{-1}] (at ρ=0.07054)	0.3222	0.30099	0.2895	0.2846
Stopping Power [MeVcm^{-1}] (at ρ=0.07078)	0.3233	0.3020	0.29048	0.2855
Stopping Power [MeVcm^{-1}] (at ρ=0.0708)	0.3234	0.3021	0.29056	0.2856

tion cooling with a unique level of precision and detail. The PID performance of the detectors is summarised in table 7 and table 8.

Detector	**Characteristic**	**Performance**
Time-of-Flight	time resolution	0.10 ns
KLOE-Light	muon PID efficiency	99 %
Electron Muon Ranger	electron PID efficiency	98.6 %
Trackers	track finding efficiency	>98 %

Table 7: Summary of the MICE detectors PID.

	KL efficiency			**EMR efficiency**		**Track finding efficiency**					
						3 mm		6 mm		10 mm	
Momentum	electrons	muons	pions	electrons	muons	US	DS	US	DS	US	DS
140 MeV/c	95 %	97 %	n.a.	98 %	35 %			98 %	99 %	98 %	99 %
170 MeV/c	95 %	99 %	89 %	99 %	99 %						
200 MeV/c	94 %	99 %	95 %	100 %	99 %	99 %	96 %	99 %	96 %		
240 MeV/c	96 %	99 %	97 %	99 %	99 %						
300 MeV/c	95 %	99 %	98 %	n.a.	99 %						

Table 8: Summary of the MICE detectors PID for different beam settings.

All the different elements of the MICE instrumentation have been used to characterise the beam and the measurement of the cooling performance for a different variety of beam momenta, emittance, and absorbers. The experiment has thus demonstrated a technique critical for a muon collider and a neutrino factory and therefore brings those facilities one step closer.

9 Acknowledgements

The work described here was made possible by grants from the Department of Energy and National Science Foundation (USA), the Instituto Nazionale di Fisica Nucleare (Italy), the Science and Technology Facilities Council (UK), the European Community under the European Commission Framework Programme 7, the Japan Society for the Promotion of Science and the Swiss National Science Foundation, in the framework of the SCOPES programme, whose support we gratefully acknowledge. We acknowledge the use of Grid computing resources deployed and operated by GridPP in the UK [46]. We are also grateful to the staff of ISIS for the reliable operation of ISIS.

References

[1] D. V. Neuffer and R. B. Palmer, "A High-Energy High-Luminosity $\mu^+ - \mu^-$ Collider," *Conf. Proc.* **C940627** (1995) 52–54.

[2] R. B. Palmer, "Muon Colliders," *Rev. Accel. Sci. Tech.* **7** (2014) 137–159.

[3] S. Geer, "Neutrino beams from muon storage rings: Characteristics and physics potential," *Physical Review D* **57** no. 11, (Jun, 1998) 6989–6997, arXiv:hep-ph/9712290 [hep-ph].

[4] **ISS Physics Working Group** Collaboration, A. Bandyopadhyay *et al.*, "Physics at a future Neutrino Factory and super-beam facility," *Rept. Prog. Phys.* **72** (2009) 106201, arXiv:0710.4947 [hep-ph].

[5] M. Apollonio *et al.*, "Oscillation physics with a neutrino factory," hep-ph/0210192.

[6] S. Y. Lee, *Accelerator Physics (Third Edition).* World Scientific Publishing Co, 2012.

[7] S. Schröder, R. Klein, N. Boos, M. Gerhard, R. Grieser, G. Huber, A. Karafillidis, M. Krieg, N. Schmidt, T. Kühl, R. Neumann, V. Balykin, M. Grieser, D. Habs, E. Jaeschke, D. Krämer, M. Kristensen, M. Music, W. Petrich, D. Schwalm, P. Sigray, M. Steck, B. Wanner, and A. Wolf, "First laser cooling of relativistic ions in a storage ring," *Phys. Rev. Lett.* **64** (Jun, 1990) 2901–2904. http://link.aps.org/doi/10.1103/PhysRevLett.64.2901.

[8] J. S. Hangst, M. Kristensen, J. S. Nielsen, O. Poulsen, J. P. Schiffer, and P. Shi, "Laser cooling of a stored ion beam to 1 mk," *Phys. Rev. Lett.* **67** (Sep, 1991) 1238–1241. http://link.aps.org/doi/10.1103/PhysRevLett.67.1238.

[9] P. J. Channell, "Laser cooling of heavy ion beams," *Journal of Applied Physics* **52** no. 6, (1981) 3791–3793, http://dx.doi.org/10.1063/1.329218. http://dx.doi.org/10.1063/1.329218.

[10] J. Marriner, "Stochastic cooling overview," *Nucl. Instrum. Meth.* **A532** (2004) 11–18, arXiv:physics/0308044 [physics].

[11] V. V. Parkhomchuk and A. N. Skrinsky, "Electron cooling: 35 years of development," *Physics-Uspekhi* **43** no. 5, (2000) 433–452. http://stacks.iop.org/1063-7869/43/i=5/a=R01.

[12] A. N. Skrinsky and V. V. Parkhomchuk, "Cooling Methods for Beams of Charged Particles. (In Russian)," *Sov. J. Part. Nucl.* **12** (1981) 223–247. [Fiz. Elem. Chast. Atom. Yadra12,557(1981)].

[13] D. Neuffer, "Principles and Applications of Muon Cooling," *Part. Accel.* **14** (1983) 75–90.

[14] **MICE** Collaboration, M. Bogomilov *et al.*, "Demonstration of cooling by the Muon Ionization Cooling Experiment," *Nature* **578** (2020) 53–59, arXiv:1907.08562 [physics.acc-ph].

[15] M. Bonesini, "The design of MICE TOF0 detector," *MICE Note 145* (2006) . http://mice.iit.edu/micenotes/public/pdf/MICE0145/MICE0145.pdf.

[16] R. Bertoni *et al.*, "The construction and laboratory tests for MICE TOF0/1 detectors," *MICE Note 241* (2008) . http://mice.iit.edu/micenotes/public/pdf/MICE0241/MICE0241.pdf.

[17] R. Bertoni *et al.*, "The design and commissioning of the MICE upstream time-of-flight system," *Nuclear Instruments and Methods in Physics Research A* **615** (Mar., 2010) 14–26, `arXiv:1001.4426 [physics.ins-det]`.

[18] R. Bertoni *et al.*, "The construction of the MICE TOF2 detector," *MICE Note 286* (2010) . `http://mice.iit.edu/micenotes/public/pdf/MICE0286/MICE0286.pdf`.

[19] D. Adams *et al.*, "Pion contamination in the MICE muon beam," *Journal of Instrumentation* **11** (Mar., 2016) P03001, `arXiv:1511.00556 [physics.ins-det]`.

[20] **MICE** Collaboration, M. Bogomilov *et al.*, "The MICE Muon Beam on ISIS and the beam-line instrumentation of the Muon Ionization Cooling Experiment," *JINST* **7** (2012) P05009, `arXiv:1203.4089 [physics.acc-ph]`.

[21] **MICE** Collaboration, D. Adams *et al.*, "Characterisation of the Muon Beams for the Muon Ionisation Cooling Experiment," *Eur. Phys. J. C* **73** no. 10, (2013) 2582, `arXiv:1306.1509 [physics.acc-ph]`.

[22] D. Adams *et al.*, "Electron-muon ranger: performance in the MICE muon beam," *Journal of Instrumentation* **10** (Dec., 2015) P12012, `arXiv:1510.08306 [physics.ins-det]`.

[23] **MICE** Collaboration, D. Adams *et al.*, "First particle-by-particle measurement of emittance in the Muon Ionization Cooling Experiment," *Eur. Phys. J. C* **79** no. 3, (2019) 257, `arXiv:1810.13224 [physics.acc-ph]`.

[24] Y. Karadzhov *et al.*, "TOF detectors Time Calibration," *MICE Note 251* (2009) . `http://mice.iit.edu/micenotes/public/pdf/MICE0251/MICE0251.pdf`.

[25] L. Cremaldi, D. A. Sanders, P. Sonnek, D. J. Summers, and J. Reidy, Jim, "A Cherenkov Radiation Detector with High Density Aerogels," *IEEE Trans. Nucl. Sci.* **56** (2009) 1475–1478, `arXiv:0905.3411 [physics.ins-det]`.

[26] L. Cremaldi *et al.*, "Progress on Cherenkov Reconstruction in MICE," *MICE Note 473* (2015) . `http://mice.iit.edu/micenotes/public/pdf/MICE0473/MICE0473.pdf`.

[27] F. Ambrosino *et al.*, "Calibration and performances of the KLOE calorimeter," *Nucl. Instrum. Meth. A* **598** (2009) 239–243.

[28] R. Asfandiyarov *et al.*, "The design and construction of the MICE Electron-Muon Ranger," *Journal of Instrumentation* **11** (Oct., 2016) T10007, `arXiv:1607.04955 [physics.ins-det]`.

[29] F. Drielsma, "Electron-Muon Ranger: hardware characterization," Master's thesis, University of Geneva, 2014. `https://arxiv.org/abs/1710.06946`.

[30] F. Drielsma, *Measurement of the Increase in Phase Space Density of a Muon Beam through Ionization Cooling*. PhD thesis, University of Geneva, 10, 2018.

[31] M. Ellis *et al.*, "The Design, construction and performance of the MICE scintillating fibre trackers," *Nucl. Instrum. Meth.* **A659** (2011) 136–153, `1005.3491`.

[32] **D0** Collaboration, V. M. Abazov *et al.*, "The Upgraded D0 detector," *Nucl. Instrum. Meth.* **A565** (2006) 463–537, `physics/0507191`.

[33] A. Dobbs *et al.*, "The reconstruction software for the MICE scintillating fibre trackers," *JINST* **11** no. 12, (2016) T12001, arXiv:1610.05161 [physics.ins-det].

[34] F. Drielsma, "Beam-based detector alignment in the MICE muon beam line," arXiv:1805.06623 [physics.ins-det]. https://arxiv.org/abs/1805.06623.

[35] V. Bayliss *et al.*, "The liquid-hydrogen absorber for mice," *Journal of Instrumentation* **13** no. 09, (2018) T09008. http://stacks.iop.org/1748-0221/13/i=09/a=T09008.

[36] "Cernox RTDs [Accessed 2 Oct. 2018],". https://www.lakeshore.com/Documents/LSTC_Cernox_l.pdf.

[37] "Temperature Measurement and Control Catalog [Accessed 2 Oct. 2018],". https://www.lakeshore.com/Documents/LakeShoreTC_l.pdf.

[38] C. Brown *et al.*, "Systematic Uncertainties in the lH2 absorber," *MICE Note 524* (2018) . http://mice.iit.edu/micenotes/public/pdf/MICE0524/MICE0524.pdf.

[39] G. Hardin, "Aluminum 6061-T6 (UNS AA96061) [Accessed 3 Oct. 2018],". https://www.nist.gov/mml/acmd/aluminum-6061-t6-uns-aa96061.

[40] S. Ishimoto *et al.*, "Liquid Hydrogen Absorber for MICE," *Conf. Proc.* **C100523** (2010) 421–423.

[41] M. Green *et al.*, "Does One Know the Properties of a MICE Solid or Liquid Absorber to Better than 0.3 Percent?," *MICE Note 155* (2006) . http://mice.iit.edu/micenotes/public/pdf/MICE0155/MICE0155.pdf.

[42] "Atomic and nuclear properties of aluminum,". http://pdg.lbl.gov/2017/AtomicNuclearProperties/HTML/aluminum_Al.html.

[43] "Atomic and nuclear properties of liquid hydrogen,". http://pdg.lbl.gov/2017/AtomicNuclearProperties/HTML/liquid_hydrogen.html.

[44] "Muon in aluminum,". http://pdg.lbl.gov/2017/AtomicNuclearProperties/MUE/muE_aluminum_Al.pdf.

[45] "Muons in liquid hydrogen,". http://pdg.lbl.gov/2017/AtomicNuclearProperties/MUE/muE_liquid_hydrogen.pdf.

[46] D. Britton *et al.*, "Gridpp: The uk grid for particle physics," *Philosophical transactions. Series A, Mathematical, physical, and engineering sciences* **367** (07, 2009) 2447–57.